

## Coupled CFD/CSD Simulations of Dust Production by Fragmenting Charges Using Stabilized Linear Elements

Dr. Orlando A. Soto; Applied Simulations Inc. (ASI); McLean, Virginia, USA

Dr. Joseph D. Baum; Applied Simulations Inc. (ASI); McLean, Virginia, USA

Prof. Rainald Löhner; George Mason University; Fairfax, Virginia, USA

Keywords: Stabilization, mixed strain/displacement formulation, CFD/CSD coupled problems, air-blast, blast propagation, numerical simulations, dust effects.

### Abstract

This paper presents a mixed Strain/Displacement Finite Element (FE) approach, which has been used for fracture computation in strongly coupled blast problems. The main difference with the standard irreducible formulation (displacement-based formulations) is that the tensorial strain field is one of the main FE variables of the discretized problem, hence, its rate of convergence is one order higher than the strain field obtained from standard displacement formulations. Since the strain (or strain rate) is the main variable to compute damage and fracture of materials, a more accurate computation of such a field gives more confident results in practical problems. Furthermore, numerical experience has shown that low order approximation of the strain field may produce totally non-physical and mesh dependent fracture results. An additional benefit of the mixed strain/displacement formulation presented below, is that it is stable for linear elements, which are very attractive due to its low computational cost, and its relatively fast pre-processing stage (CAD and mesh generation).

Finally, the paper analyses and compares the numerical results of a coupled Computational Fluid Dynamics (CFD) / Coupled Structural Dynamics (CSD) blast simulation with experimental data. The simulation consisted of the response of two reinforced concrete walls to loads from a cased charge, placed in close proximity to the center of one of the walls. This real-life case also shows the importance of taking into account the dust production due to the concrete fragmentation, which absorbs energy from the flow, and damps in a very dramatic way the shock strength.

### Introduction

Theoretical modeling and computational resolution of the strain localization process up to structural failure remains an open challenge in computational solid dynamics (CSD). To date, most attempts to model discontinuities with standard local approaches produce non-physical solutions, which are fully determined by mesh resolution and orientation. Cervera et al. (see [1]) showed this must be due to the poorly numerical approximation that is obtained if irreducible formulations are used (standard displacement formulations). The previous statement may be simply explained by taking into account that in irreducible formulations, the strain, which is the variable of most interest for fracture prediction, are obtained by differentiation of the fundamental unknowns (the displacement field). Hence, if linear (or trilinear) FE are used, the strain field has a theoretical convergence of order  $O(h)$  in  $L_2$ -norm ( $h$  is the mesh size). Therefore, the strain field has zero point convergence order (in  $L_\infty$ -norm), which means that even though the mesh resolution is improved, point values do not converge. Since point strains and/or stresses (values at integration points) are used to predict material damage and element fracture, it is of no surprise that localization bands strongly depends on the mesh size and orientation. Contrariwise, when using the strain and displacement fields as primary variables of the formulation, the added accuracy and convergence seems to be enough to satisfactorily solve the mentioned mesh dependency problem (see [1] and references therein).

Herein an explicit, strain/displacement, large-deformation FE formulation to deal with strong coupled CFD/CSD (computational fluid dynamics/computational solid dynamics) problems is presented. It is widely known that, if standard equal interpolation is used for the spatial discretization of both fields, strain and displacement, the scheme locks and produces meaningless and non-stable results since the inf-sup condition is not fulfilled. However, equal continuous FE functions are highly desirable from a computational point of view. Therefore, to circumvent the severe restrictions imposed by such a mathematical condition, in this work the weak forms of the mixed strain/displacement solid dynamic equations are obtained by a variational multiscale stabilization (VMS) approach. Time discretization of the final continuous forms is achieved by an explicit Newmark scheme, and the spatial one by using Q1/Q1 (hexahedrons) or P1/P1 (tetrahedrons) standard functions. Several VMS methods were developed in [1-3] for the small-deformation static solid equations, and successfully applied to localization problems: Totally physical and mesh independent solutions were obtained where the standard displacement formulation failed miserably.

Finally, the CSD approach is loosely coupled with the widely tested CFD code FEFLO to solve real blast and impact problems (see [4]). A benchmark case and one real application with dust production is presented.

### Theoretical Aspects

The strong form of the continuous solid dynamics problem can be stated as:

$$\rho \ddot{\mathbf{u}} - \nabla \cdot \boldsymbol{\sigma} = \mathbf{f} \quad \text{in } \Omega_t \quad (1)$$

$$\dot{\boldsymbol{\sigma}} = \dot{\boldsymbol{\sigma}} + \dot{\boldsymbol{\sigma}}_G \quad (2)$$

$\Omega_t$ : Domain occupied by the solid at time  $t$ ;  $\rho$ : Density;  $\ddot{\mathbf{u}}$ : Acceleration;  $\boldsymbol{\sigma}$ : Stress tensor;  $\mathbf{f}$ : External forces;  $\dot{\boldsymbol{\sigma}}$ : Total time derivative of the stress tensor;  $\dot{\boldsymbol{\sigma}}$ : Co-rotational stress rate (Jaumann-Zaremba for this work);  $\dot{\boldsymbol{\sigma}}_G$ : Geometric stress update.

The constitutive material equation is replaced in equation (2) to obtain:

$$\dot{\boldsymbol{\sigma}} = \mathbf{C} : \dot{\boldsymbol{\varepsilon}} + \dot{\boldsymbol{\sigma}}_G \quad (3)$$

$\mathbf{C}$ : Constitutive material tensor;  $\dot{\boldsymbol{\varepsilon}}$ : Eulerian strain rate tensor.

Which, after time integration, may be written as:

$$\boldsymbol{\sigma}(t + \delta t) = \mathbf{C} : \boldsymbol{\delta \varepsilon} + \boldsymbol{\delta \sigma}_G + \boldsymbol{\sigma}(t) \quad (4)$$

$\boldsymbol{\delta}(\cdot)$  is defined as  $(\cdot)(t + \delta t) - (\cdot)(t)$

Hence, the final strong form to be solved may be stated as:

$$\rho \ddot{\mathbf{u}} - \nabla \cdot (\mathbf{C} : \boldsymbol{\delta \varepsilon}) - \nabla \cdot \boldsymbol{\delta \sigma}_n = \mathbf{f} \quad (5)$$

$\boldsymbol{\delta \sigma}_n$  is defined as  $\boldsymbol{\delta \sigma}_G + \boldsymbol{\sigma}(t)$

Equation 5 is the classical irreducible continuous problem expression to be solved, which, as it was already mentioned, shows very poor strain (i.e. damage and fracture field) point convergence, when low order elements are used. To improve such a shortcoming, the previous strong form may be re-written in a way that the strain field becomes a main variable of the problem, hence, its convergence rate and accuracy will increase at least one order. This improves the fracture approximation since the strain is the main variable used for most (or all) material models to compute the damage (fracture) field.

Therefore, the strong problem that is addressed in this work is stated as: Find the strain and displacement field such that

$$-\nabla \cdot (\mathbf{C} : \boldsymbol{\delta \varepsilon}) - \nabla \cdot \boldsymbol{\delta \sigma}_n = \mathbf{f} \quad (6)$$

$$-\boldsymbol{\delta \varepsilon} + \nabla^s \boldsymbol{\delta \mathbf{u}} = \mathbf{0} \quad (7)$$

$\nabla^s(\cdot)$  is the spatial symmetric gradient operator

Where the dynamic term has been dropped for shortness (a standard stable time integration is used for the final space-discretized form).

### Classical space discretization

The standard Galerkin continuous weak form of the previous strong problem may be written as: Find the strain and displacement field such that

$$(\nabla^s \mathbf{v}, \mathbf{C} : \boldsymbol{\delta \varepsilon}) + (\nabla^s \mathbf{v}, \boldsymbol{\delta \sigma}_n) = (\mathbf{v}, \mathbf{f}) + (\mathbf{v}, \mathbf{t})_{\Gamma_N} \quad (8)$$

$$-(\boldsymbol{\gamma}, \boldsymbol{\delta \varepsilon}) + (\boldsymbol{\gamma}, \nabla^s \boldsymbol{\delta \mathbf{u}}) = 0 \quad (9)$$

$\mathbf{v}$  and  $\boldsymbol{\gamma}$  are the test functions associated to the equilibrium equation (6), and to the compatibility equation (7), respectively.  $(\cdot, \cdot)$  is the scalar product in  $L_2$  over  $\Omega_t$  and  $(\cdot, \cdot)_{\Gamma_N}$  the scalar product in  $L_2$  over  $\Gamma_N$

For all functions that belong to the proper functional spaces (functions which have the right continuity over the domain to ensure the existence of the integrals). It is widely known that an Inf-Sup compatibility condition (see [1] and references therein) is required to ensure the existence and stability of the above problem, which forbid the use of standard equal

interpolation for both fields: displacements and strains. Hence, if low order standard elements (i.e. linear or bi-linear cheap elements) are used, the final discrete approximation is unstable, and only high order sophisticated non-equal interpolations can be used. To overcome such a very expensive computational approaches, sub-grid scale stabilization is used in this work as is exposed below.

### Sub-grid Scale stabilization

The basic idea behind any sub-grid scale stabilization is to enrich the standard FE spaces with functional ones that take into account the scales of the solution, which cannot be approximated by the FE computational grid. Following this idea, the test and variable functions may be extended as follows:

$$\delta \mathbf{u} = \delta \mathbf{u}_h + \delta \tilde{\mathbf{u}} \quad (10)$$

$$\delta \boldsymbol{\varepsilon} = \delta \boldsymbol{\varepsilon}_h + \delta \tilde{\boldsymbol{\varepsilon}} \quad (11)$$

$$\mathbf{v} = \mathbf{v}_h + \tilde{\mathbf{v}} \quad (12)$$

$$\boldsymbol{\gamma} = \boldsymbol{\gamma}_h + \tilde{\boldsymbol{\gamma}} \quad (13)$$

$\mathbf{a}_h$  is the component of the field  $\mathbf{a}$  on the (coarse) FE mesh, and  $\tilde{\mathbf{a}}$  is the enhancement of  $\mathbf{a}$  corresponding to the (finer) sub-grid scale.

After introducing equations 10-13 into the weak form given by equations 8 and 9, the following variational formulation is obtained:

$$(\nabla^s \mathbf{v}, \mathbf{C} : \delta \boldsymbol{\varepsilon}_h) + (\nabla^s \mathbf{v}, \mathbf{C} : \delta \tilde{\boldsymbol{\varepsilon}}) + (\nabla^s \mathbf{v}, \delta \boldsymbol{\sigma}_n) = (\mathbf{v}, \mathbf{f}) \quad (14)$$

$$-(\boldsymbol{\gamma}, \delta \boldsymbol{\varepsilon}_h) - (\boldsymbol{\gamma}, \delta \tilde{\boldsymbol{\varepsilon}}) + (\boldsymbol{\gamma}, \nabla^s \delta \mathbf{u}_h) - (\nabla \cdot \boldsymbol{\gamma}, \delta \tilde{\mathbf{u}}) = \mathbf{0} \quad (15)$$

$$-(\tilde{\mathbf{v}}, \nabla \cdot (\mathbf{C} : \delta \boldsymbol{\varepsilon}_h)) - (\tilde{\mathbf{v}}, \nabla \cdot (\mathbf{C} : \delta \tilde{\boldsymbol{\varepsilon}})) - (\tilde{\mathbf{v}}, \nabla \cdot \delta \boldsymbol{\sigma}_n) = (\tilde{\mathbf{v}}, \mathbf{f}) \quad (16)$$

$$-(\tilde{\boldsymbol{\gamma}}, \delta \boldsymbol{\varepsilon}_h) - (\tilde{\boldsymbol{\gamma}}, \delta \tilde{\boldsymbol{\varepsilon}}) + (\tilde{\boldsymbol{\gamma}}, \nabla^s \delta \mathbf{u}_h) + (\tilde{\boldsymbol{\gamma}}, \nabla^s \delta \tilde{\mathbf{u}}) = \mathbf{0} \quad (17)$$

It can be noticed that expressions 16 and 17 are not anything else but projections of the standard FE residuals onto the sub-scales (sub-grid) spaces, which cannot be resolved by the FE mesh. Now, the problem is how to calculate these projections. By using an approximate Fourier analysis of the problem (see [1, 5] for details), it can be shown that:

$$\delta \tilde{\boldsymbol{\varepsilon}} = \tau_\varepsilon \tilde{\mathbf{P}}_\varepsilon [\nabla^s \delta \mathbf{u}_h - \delta \boldsymbol{\varepsilon}_h] \quad (18)$$

$$\delta \tilde{\mathbf{u}} = \tau_u \tilde{\mathbf{P}}_u [\nabla \cdot (\mathbf{C} : \delta \boldsymbol{\varepsilon}) + \nabla \cdot \delta \boldsymbol{\sigma}_n + \mathbf{f}] \quad (19)$$

$\tilde{\mathbf{P}}_\varepsilon, \tilde{\mathbf{P}}_u$  are projections onto the sub-grid scale spaces of  $\tilde{\boldsymbol{\varepsilon}}$  and  $\tilde{\mathbf{u}}$ , respectively; and  $\tau_\varepsilon, \tau_u$  are the stabilization parameters.

The way the projection is taken will end up in different sub-grid methods. For the ASGS (Algebraic Sub-Grid Scale) approach, the standard FE term is taken as the projection (identity or Galerkin least-square projection). However, even though the final ASGS weak form is consistent at continuous level, the discrete one is not in a strictly manner. For that reason, in this work the OSS (Orthogonal Sub-Grid Scale) method is used, which enforces consistency not only at continuous level but also at discrete one: Whatever term is added at the standard discrete form, is also subtracted as is shown below.

The OSS approach takes the orthogonal projection of the residual (standard FE term minus its projection) to approximate the right-hand side terms of 18-19. Hence, the final OSS variational form that was implemented in this work may be written as:

$$(\mathbf{v}, \rho \ddot{\mathbf{u}}) + (\nabla^s \mathbf{v}, \mathbf{C} : \delta \boldsymbol{\varepsilon}_h) + \tau_\varepsilon (\nabla^s \mathbf{v}, \mathbf{C} : (\nabla^s \delta \mathbf{u}_h - \delta \boldsymbol{\varepsilon}_h)) + (\nabla^s \mathbf{v}, \delta \boldsymbol{\sigma}_n) = (\mathbf{v}, \mathbf{f}) \quad (20)$$

$$(\boldsymbol{\gamma}, \delta \boldsymbol{\varepsilon}_h) = (\boldsymbol{\gamma}, \nabla^s \delta \mathbf{u}_h) - \tau_\varepsilon (\boldsymbol{\gamma}, \nabla^s \delta \mathbf{u}_h - \mathbf{P}(\nabla^s \delta \mathbf{u}_h)) - \tau_u (\nabla \cdot \boldsymbol{\gamma}, \nabla \cdot \boldsymbol{\sigma} - \mathbf{P}(\nabla \cdot \boldsymbol{\sigma})) \quad (21)$$

$$\tau_\varepsilon = \frac{C_\varepsilon h \mu}{L \mu_0} ; \quad \tau_u = \left( \frac{\rho}{\delta t^2} + \frac{\mu}{C_u h L} \right)^{-1} \quad (22)$$

$C_\varepsilon$  and  $C_u$  are positive constants,  $\mu$  is a mechanical parameter of the problem chosen as the ratio between the norms of the deviatoric stress and total strain tensors,  $\mu = \|\text{dev } \boldsymbol{\sigma}\| / \|\text{dev } \boldsymbol{\varepsilon}\|$ ,  $\mu_0$  its initial elastic value,  $L$  is a characteristic length of the problem and  $h$  is the size of the finite element. It easily noticed that the previous form is consistent at discrete level since

every term that is added to the standard FE formulation, is subtracted as its projection. Essentially, each additional non-Galerkin term is also subtracted by using a different approximation (its projection). Such a procedure has been widely used in the CFD (Computational Fluid Dynamics) community to stabilize incompressible flow formulations, where it is called the 4<sup>th</sup> order damping term (see ref [6] for details). The expressions for the stabilization parameters given by (22), have been chosen according to the optimal convergence results obtained for equal interpolation in [1-3, 5].

### Numerical Benchmark

As follows, the previous formulation is tested with the Cook Membrane benchmark which is shown in Figure 1.

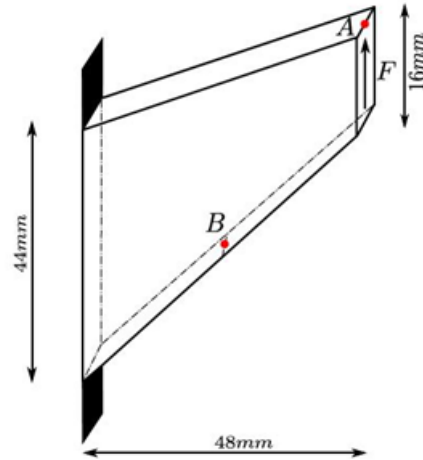


Figure 1. Cook Membrane Geometry.

It is well known that the irreducible formulation locks for quasi-incompressible elastic cases (Poisson ratio close to 0.5). Hence, in this work a Poisson ratio of 0.4999 is used to test the presented formulation. The material Young Modulus is taken as 200 GPa, and its density as  $10^4 \text{ Kg/m}^3$ . Both stability constants (see Eq. 22)  $C_\epsilon$  and  $C_u$  are taken as 1.0.

Figure 2 compares the vertical displacement of point A (see Figure 1) obtained by the OSS stabilized element (red curve), the widely use hourglass stabilized element of Flanagan and Belytschko [7] (green curve), and the irreducible standard FE formulation (blue curve).

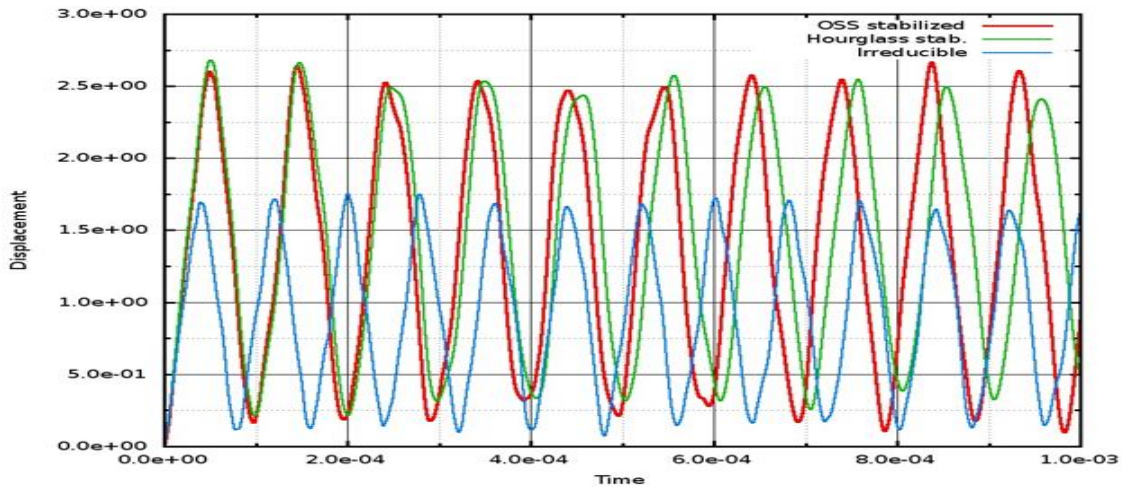


Figure 2. Vertical displacement of point A using the OSS strain/displacement formulation (red), the irreducible formulation discretized with the Flanagan Belytschko one point integrated element with hourglass viscosity (green), and the standard irreducible FE formulation (blue).

It is well known by the CSD (Computational Solid Dynamic) community that the Flanagan/Belytschko (FB) element does not show locking for quasi-incompressible applications (i.e. isochoric plasticity). Hence, based on the results presented above (Fig. 2), the OSS stabilized formulation is also suitable for such applications. Essentially, it produces very similar displacement than the FB element. On the contrary, the standard irreducible formulation totally locks for this benchmark (see Fig.2). It produces a maximum vertical displacement which is half of the expected one.

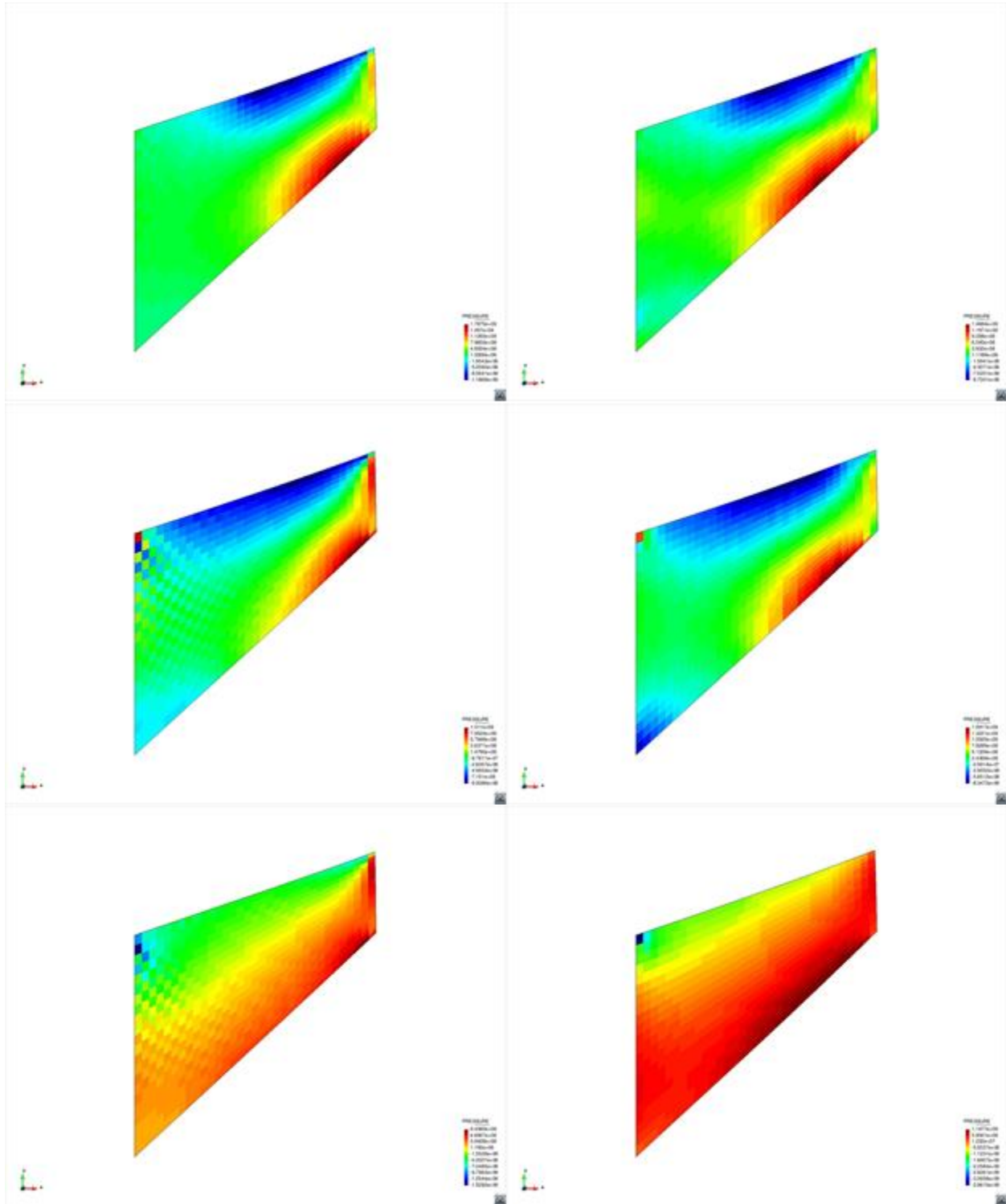


Figure 3. Mechanical pressure (average main stress field). Left: FB element. Right: OSS formulation.

It can be argued that while the FB element needs only one integration point per element, the OSS formulation (Eq. 20-22) needs to be fully integrated (eight integration points for hexahedral elements), which makes it much more expensive from a computationally point of view. This argument is not valid if tetrahedral elements are used, since, it can be deduced from forms (20) and (21), the OSS formulation only needs one point integration rule for linear interpolations. However, for hexahedral elements (tri-linear interpolation), the additional cost pays out since the OSS formulation produces more stable and free of spurious oscillations stress (and strain) fields than the FB element, as it is shown below.

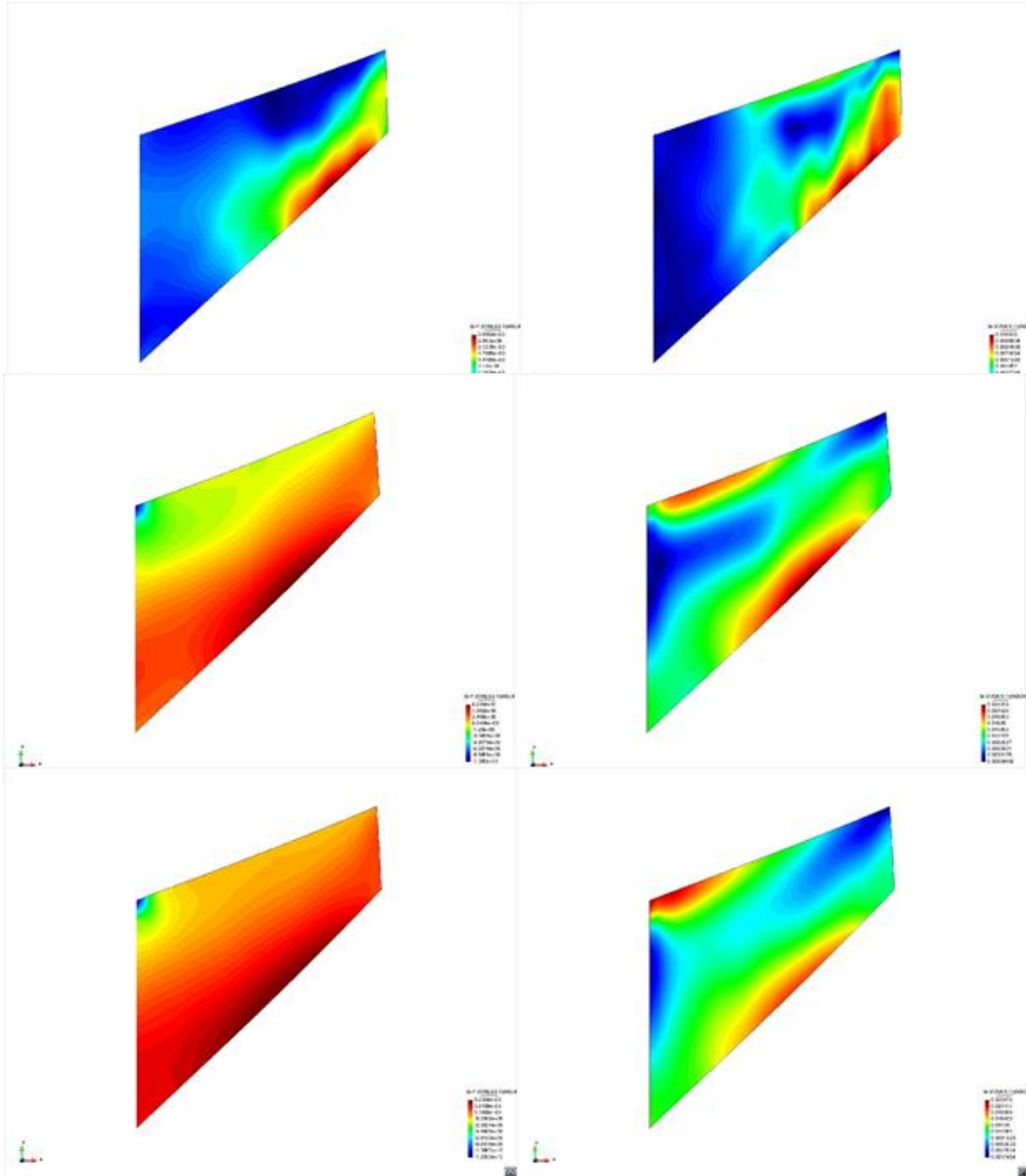


Figure 4. Principal stress (left) and strain evolution (right) for the OSS strain/displacement formulation.

Figure 3 shows the mechanical pressure (average main stress) for the OSS formulation and the FB element. It can be observed that while this variable is stable for every step of the OSS approach, the FB element shows a chess board mode instability in some time steps. Such spurious oscillations destroy the computation of the damage field, hence, the accuracy of the fracture computation. Finally, Figure 4 shows the evolution of the principal stress and strain for

the OSS formulation. It can be observed that both variables are continuous and stable for every time step, which ensure a good approximation of the damage field.

Experimental Test Application

In this section, a real test simulation which experimental data is presented. Figure 5 shows the test configuration. The test structure consisted of a disposable burst room composed of two culvert sections. A reusable thick reinforced concrete closure panel with a doorway is placed at the far end to provide confinement and controlled venting of the structure. The permanent portion of the test structure is designed to study the failure of the first wall, propagation of blast and debris into the second bay, and progressive loading and failure of the second wall. The facility incorporates two replaceable test walls, loaded with load beams to ensure full enclosure during the test. The replaceable test walls permit us to quickly reconstruct the test facility and study the effect of wall geometry, reinforcing, and material strength as well as weapon size and standoff.

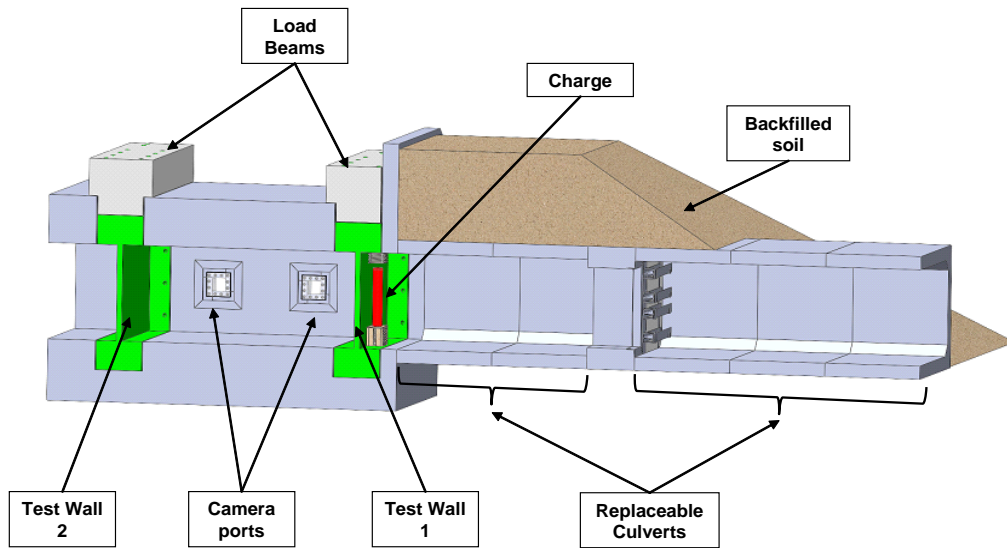


Figure 5. Test configuration.

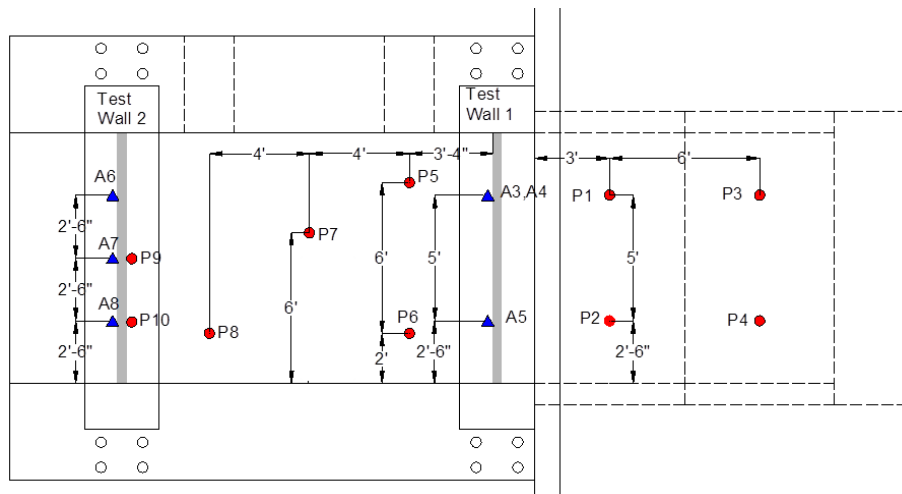


Figure 6. Test instrumentation.

Figure 6 shows the instrumentation for the test. Instrumentation in the burst room consisted of four pressure gauges on the ceiling of the culvert sections. Six additional pressure gauges were placed in Bay 2, four on the ceiling and two on the front face of the second test wall. Accelerometers, three on both test walls, provided a measure of the structural

response of the two walls. Two camera ports in Bay 2 provided high speed video of the failure and debris ejection off of wall 1. Two exterior cameras provided high speed video of the wall 2 response.

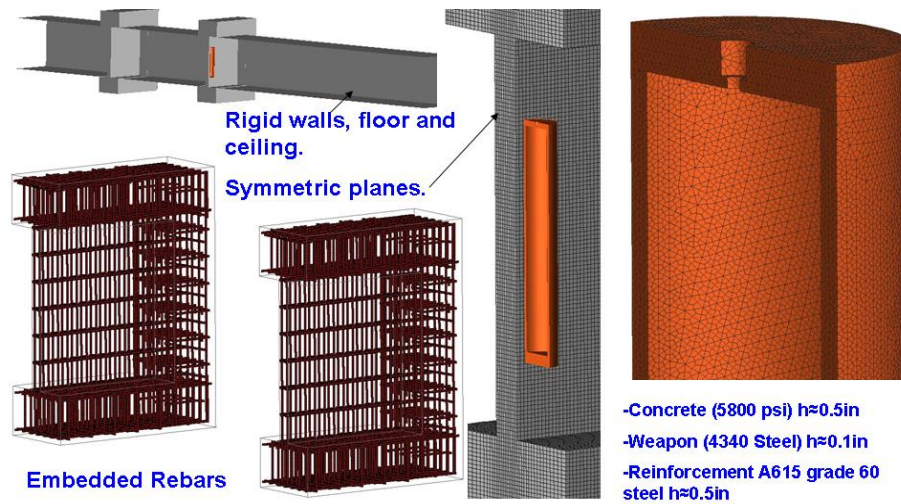


Figure 7. CSD modeling details of the test facility, explosive case, and test walls.

Figure 7 shows some of the CSD modeling details of the facility, test walls, and explosive case. The modeled facility included two rooms, the detonation room and bay room. In the initial simulation, each room's ceiling, floor and culverts were modeled as non-responding. Only the two test walls were allowed to respond. The test walls were modeled with 0.5 inch solid elements with beams used to model the rebar.

The weapon case was modeled with 0.1 inch size linear elements. The Tritonal and C4 booster explosives were both modeled with a JWL equation-of-state. Past attempts to model Tritonal using simple JWL equation-of-state were not successful. However, the latest chemical kinetics models incorporated within FEFLO (CFD solver) resulted in blast wave evolution that was in excellent agreement with the data, as will be shown later.

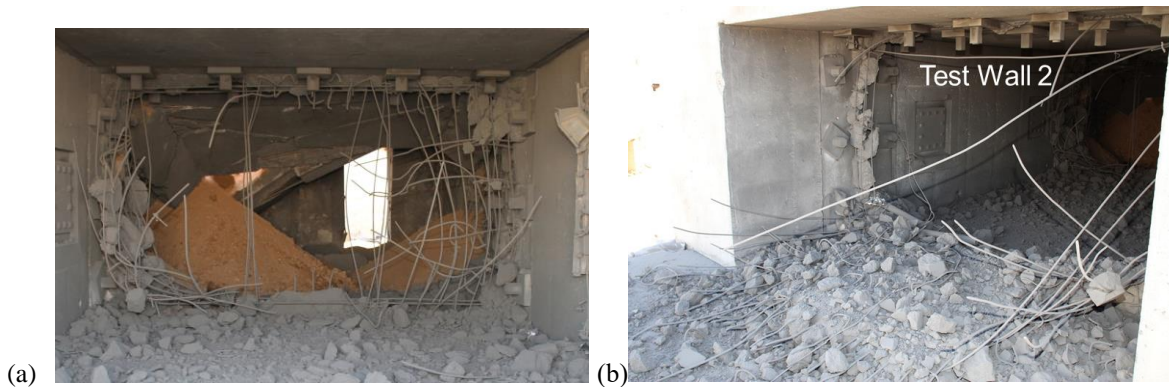


Figure 8. Post-test photographs of test walls. a. Internal view of test wall 1; b. External view of test wall 2.

Figure 8 shows the damage to the two test walls post-test. Both walls were catastrophically destroyed. A snapshot from high speed video (Fig 9a) shows that test wall 1 initially breached over the middle third of the wall, propagating blast pressure and high speed debris into the second bay. The coupled simulation, performed with the computational code FEMAP (which couples the flow solver FEFLO and the CSD solver ASICSD), replicates this initial breach as shown in Fig 9b. The simulation also agreed reasonably well on the maximum debris velocity measured from the video. Later time pressures were sufficient to fail and remove both the wing walls. Note the large chunks of debris that remained entangled in the rebar and on the floor over the front third of bay 2. The combined pressure and debris loading on test wall 2 was sufficient to fail test wall 2 which sheared at the top and rotated downward, as shown in Fig 8b.

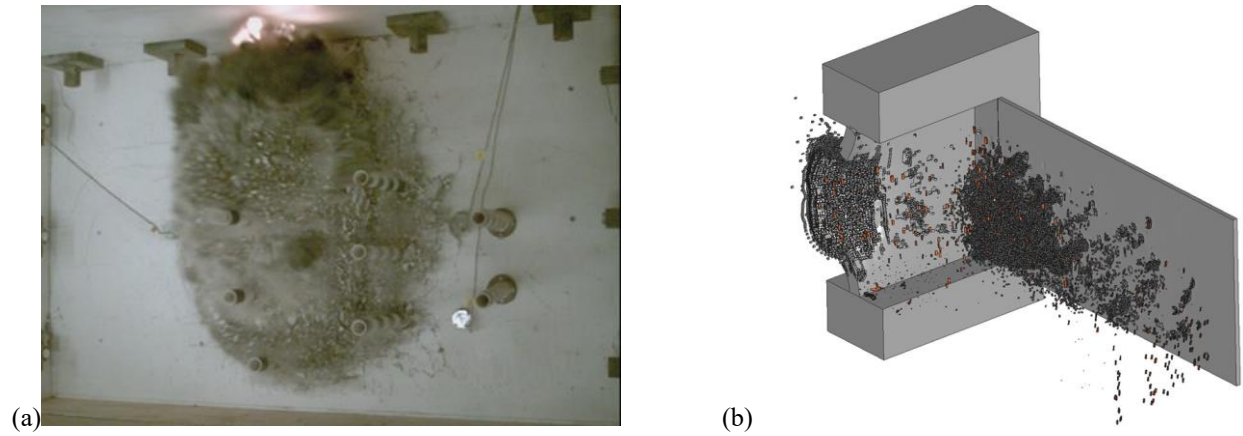


Figure 9. Initial breach of test wall 1: a. High speed video clip; b. FEMAP simulation.

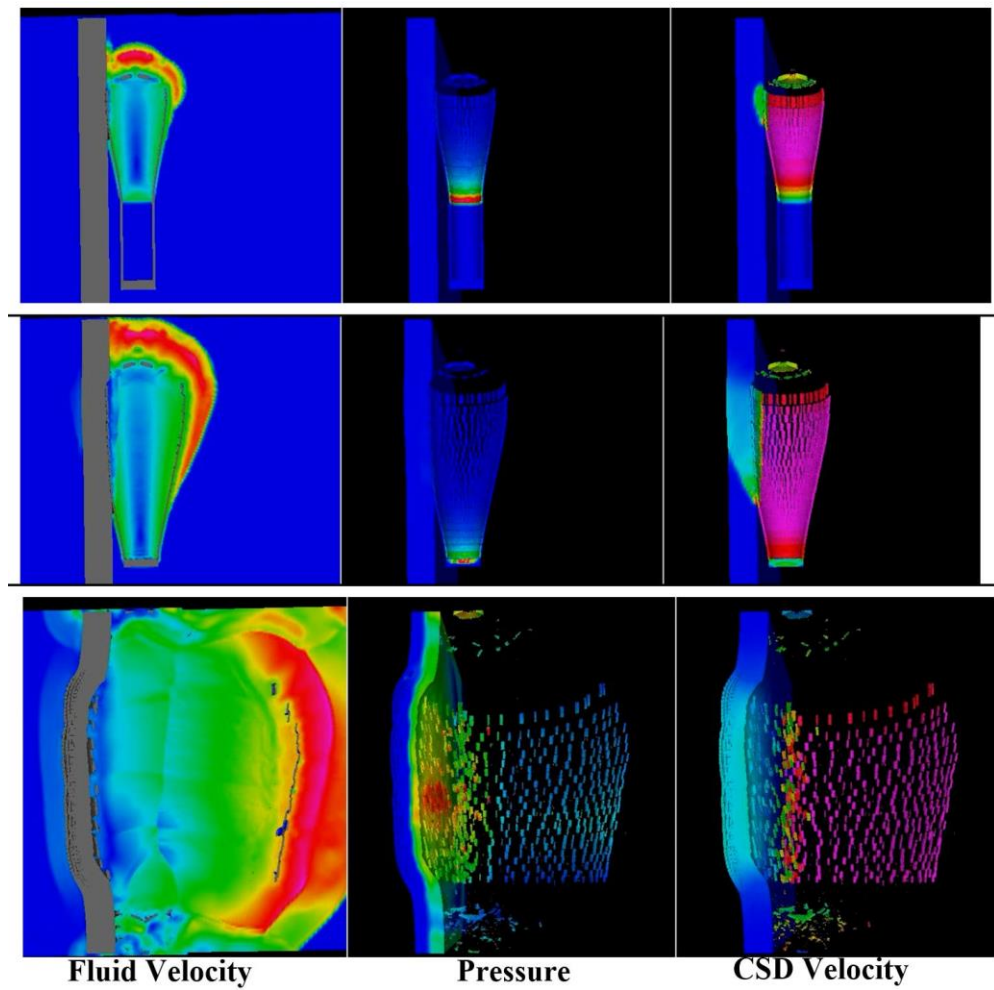


Figure 10. Detonation, case fragmentation and wall breach. Shown are the fluid velocity contours, and the resulting structural pressure and velocity at 3 times during detonation and wall breach.

Figure 10 shows a sequence of snapshots taken at three times during the detonation process: at the middle of the detonation, at the end and sometime afterwards. In each panel shown are the velocity contours on the plane of symmetry (left), the pressure on the structure (center) and the velocity of all structural elements (right). The figures exhibit: 1) the top, point detonation initiation and propagation down the explosive; 2) the case expansion and break-up (initial

case failure is at the weld between the base plate and the cylindrical charge, failing due to shear); 3) detonation products escape through the expanding cracks (notice that due to the large pressure ratio, the detonation products achieve supersonic speeds upon expansion, cooling down and thus strongly affecting the later combustion of any aluminized particles or other additives); 4) the high speed cylindrical fragment expansion and the low velocity base and tail plates fragments; and 5) wall breach. While a significant pressure load is imposed on the wall, the initial breach resulted from fragment loading, which was significantly higher than pressure loading at this time.

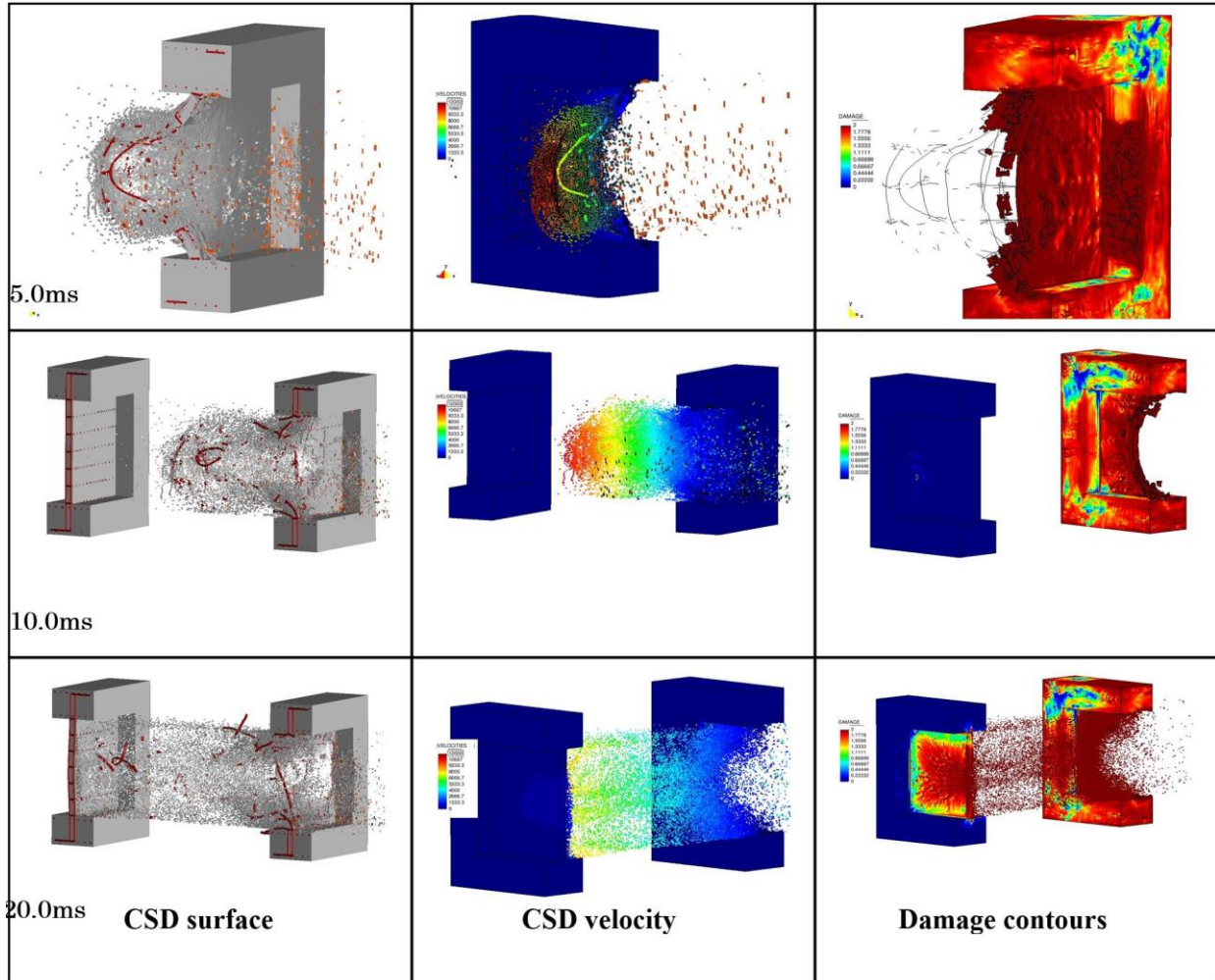


Figure 11. Test walls response at 5.0ms, 10.0ms and 20.0ms. Shown are the CSD surfaces, including secondary debris and fragments, CSD velocity and test wall damage contours.

Figure 11 shows test walls response at 5.0, 10.0 and 20.0 ms. Shown at each time are the structural surface, including the secondary debris and the breaking rebars, the structural component velocity, and the damage contour plots (where zero is non-damaged, and 2.0 is totally-damaged, i.e., the deviatoric stresses are zero, and the element can only withstand compression, but not tension or shear). The blast wave propagating through the breach has arrived to test wall 2 well before the slower-propagating secondary debris. Still, the air blast pressure loading was not sufficient to fail the wall: a large debris loading from the first wall failure contributed substantially to the failure of the second wall as observed in the test.

Comparison of pressure time histories at three locations is shown in Fig. 12. Figure 12 left shows comparison for a station in the blast room, while Fig 12 center and Fig 12 right show comparisons for stations in the bay area. In the blast room, the results show excellent agreement between the measured and predicted data in terms of shock arrival time, the ceiling-reflected shock and side-wall reflected shock. Until 10ms, all shock reverberation features are captured correctly. However, at 10ms the simulations predict the arrival of the reflected shock from the back side of the

room, opposite test wall 1, while the test results do not show this reflection. Similarly, the predictions in the bay room track the experimental data nicely until 11ms, and then deviate drastically.

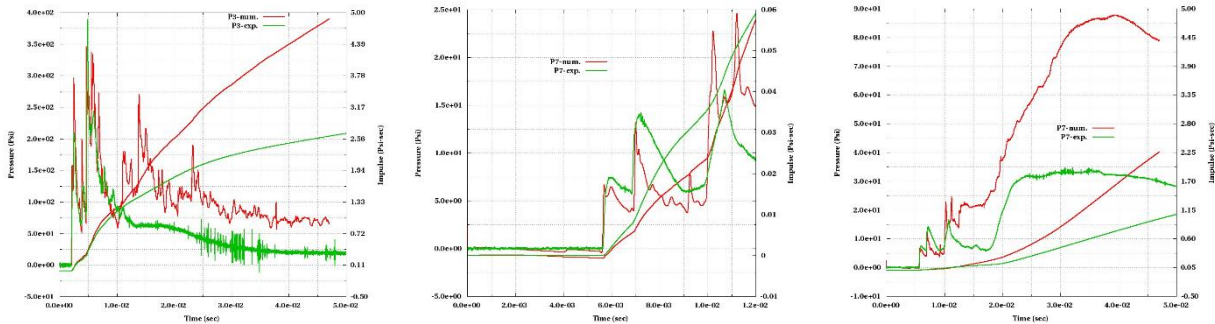


Figure 12. Comparison of measured and predicted pressure time histories at three locations, one in the detonation room and two in the Bay room.

A careful analysis of post-test results helped explain this phenomenon. The culvert post-test shots (Fig 13) indicate that weapon fragment impacts on the side culverts resulted in complete stripping of the concrete cover to the first rebar cage. We estimated the amount of concrete stripped at several hundred kilograms. This clearly indicated that modeling of the culvert as non-responding was not appropriate. Hence, we repeated the simulation this time modeling the culvert as any other reinforced concrete wall, including concrete failure and pulverization in response to the high-speed weapon fragments impact.



Figure 13. Test results show the significantly damaged east and west culverts.

Figure 14 shows the CSD surfaces and damage contours at 1.5 ms and 3.0 ms. At this early time the breach damage to the test is identical to the breach damaged obtained in the no-dust previous simulation. In addition, significant damage is now observed along the culvert side walls, due to high-speed fragment impact. The model predicted stripping of the concrete to the first layer of rebars, in agreement with the observed test results.

Figure 15 show the time evolution of dust mass injection into the room and the injection velocity. Most dust is injected within the first 6.0 ms. Since the detonation room is fairly long, there is a time span between the fragment impact near the test wall to fragment impact on the culvert at the far end of the room. The fragments impact the wall at velocities of about 1.0 km/sec, and the dust is blown off the wall with initial velocities of 300 to 600 m/s. The dust velocity decays rapidly after ejection, as the dust blown off the wall encounters the high pressure blast wave, which at these ranges, lags the case fragments.

Finally, we compare predicted and measured pressure and impulse time histories at several locations, as well as measured and predicted walls response (acceleration and deflection) for the two test walls, obtained when incorporating dust production from the culverts in the simulation. Figure 16a shows a comparison for stations 1 and 2 (symmetric) in the detonation room. The experimental data is in black, the previous no-dust prediction is in green, and the new predicted results modeling dust is in red. The difference between the predictions is strikingly evident at about 10ms, when the reflected shock from the room far end attempts to propagate towards the test walls. The reflected wave now encounters several hundred kilograms of fine dust. The reflected wave is now damped (i.e., significant energy loss)

due to: 1) thermal (internal) energy loss as the dust particles internal energy increases due to heating by the hot detonation products; and 2) drag damping (kinetic energy loss), as the blast wave accelerates the slower particles.

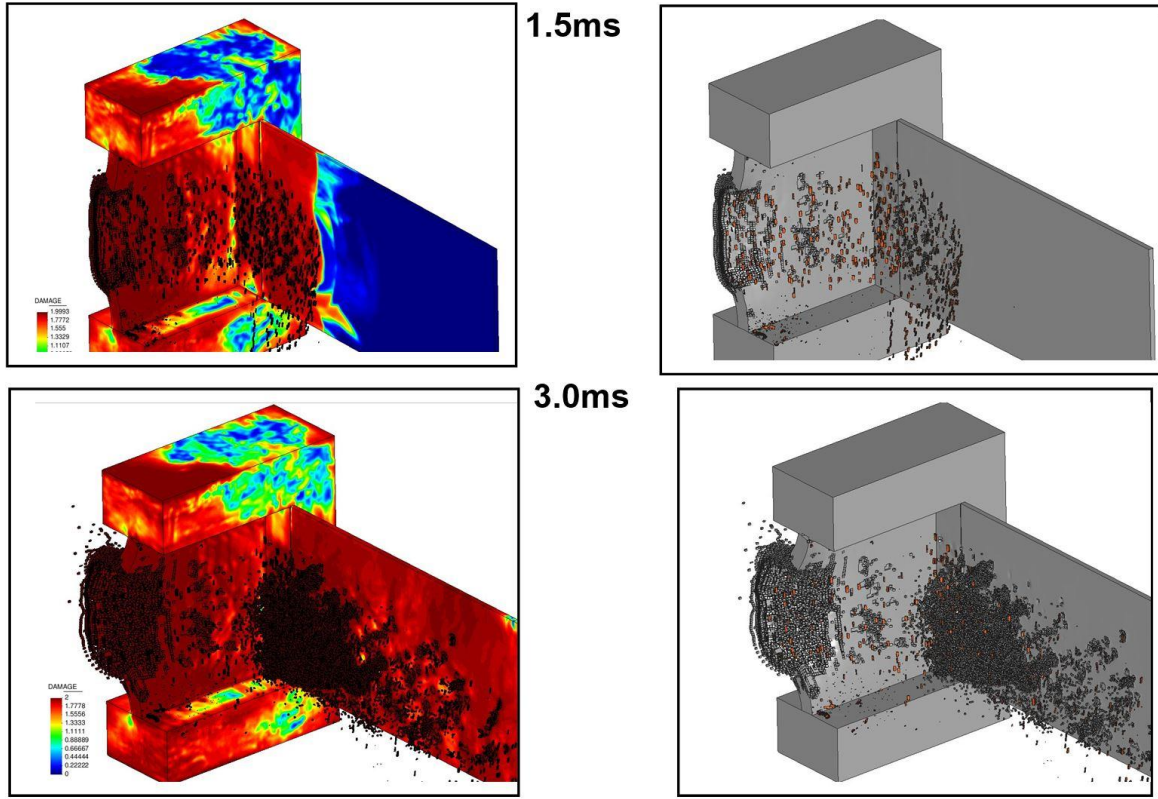


Figure 14. CSD surfaces and damage contours at 1.5 ms and 3.0 ms.

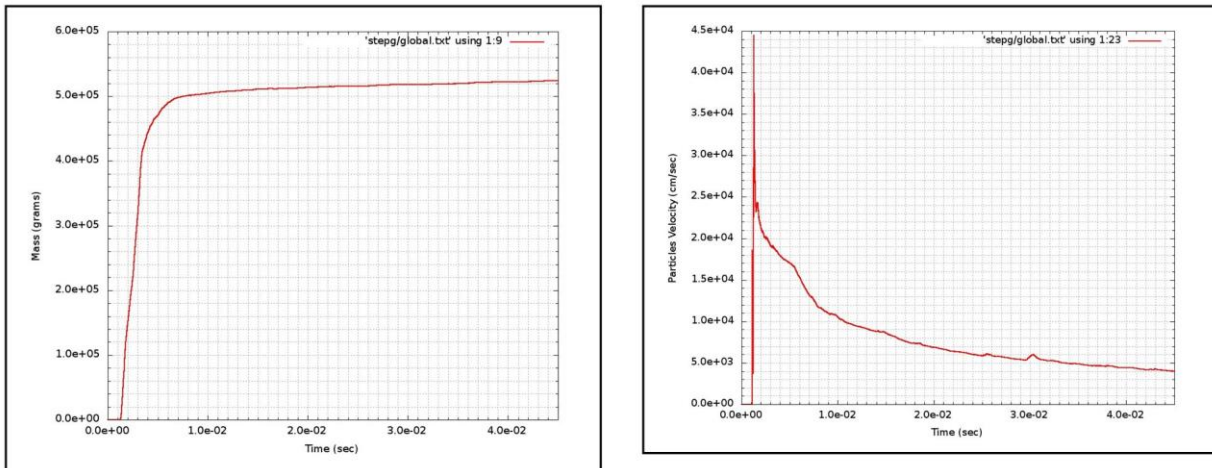


Figure 15. Temporal evolution of dust mass injection and dust velocity off the culvert walls.

The corrected description of the controlling physical processes (i.e., dust losses) yields a more accurate blast wave energy damping, as shown in Fig 16a for a station in the blast room. Similar results were obtained for two stations in the bay room: station 8 located on the ceiling, and station 10, located on test wall 2 (Figs 16b and 16c, respectively). Finally, the more accurate pressure environment prediction resulted in a more accurate structural response prediction. Figures 17a and 17b show comparisons of measured and predicted accelerations and displacements for test walls 1 and 2, respectively. Good agreement is demonstrated both in terms of acceleration and displacement.

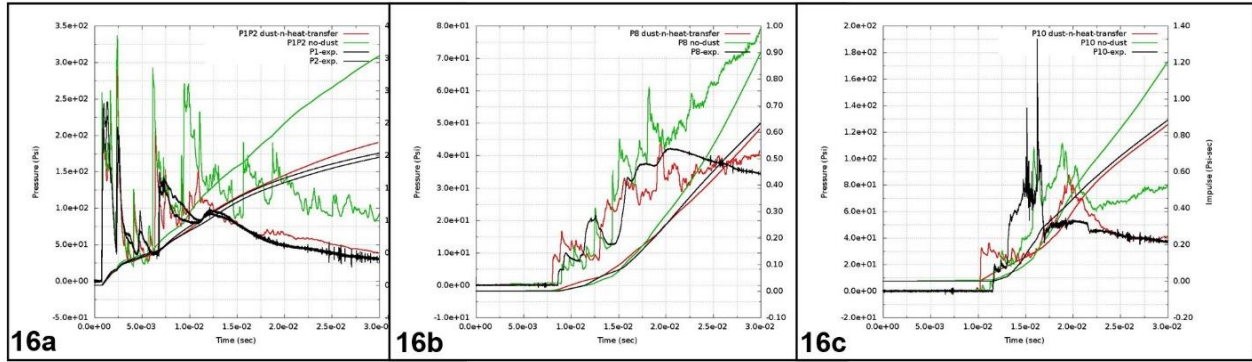


Figure 16. Comparison of measured and predicted pressure and impulse values in A. Burst room; B. On ceiling; and C. Bay 2 on Test Wall 2.

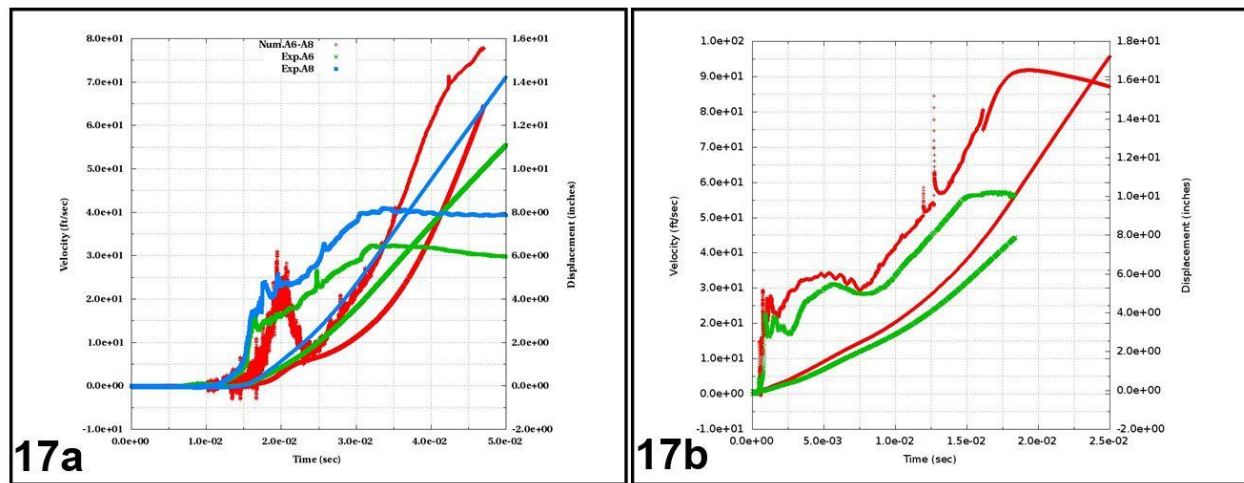


Figure 17. Comparison of measured and predicted wall motions. A. Test wall 1; b. Test wall 2.

## Conclusions

A stabilized mixed strain/displacement (strain rate/velocity) OSS formulation has been presented. The main advantage is that equal order interpolation for the strain and displacement can be accommodated, which is highly desirable from a computational point of view. In addition, the formulation allows the use of low order FE interpolations (linear and bi-linear elements), which are computationally cheap.

It was shown through the numerical benchmark, that the introduced OSS formulation is more stable and equally accurate than the widely used Flanagan Belytschko hourglass stabilized element, which has been widely used and tested in the CSD community.

From a theoretical point of view, the formulation shows one order of convergence higher than the standard displacement formulations. This hypothesis was demonstrated in a computational manner, since the irreducible formulation locks (present non-physical smaller displacements) for incompressible benchmark cases. In addition, even though the hourglass stabilized irreducible formulation (FB element) does not lock, it presents spurious stress oscillations at some time steps, which most probably will destroy the damage and fracture computation in real life applications.

Finally, a coupled fluid-structure test with abundant experimental data was simulated to validate the presented formulation. The numerical and experimental results agreed very well after taking into account the energy losses due to dust production.

## Acknowledgements

The authors gratefully acknowledge the financial support provided by the Defense Threat Reduction Agency, DTRA/J9CXSS and DTRA/J9CXT. Drs. Michael. E. Giltrud and Ali Amiri serve at the Technical Control Monitors.

## References

[1] Cervera, M., Chiumenti M., and Codina, R., (2010) "Mixed stabilized finite element methods in nonlinear solid mechanics. Part I: Formulation". *Computer Methods in Applied Mechanics and Engineering*, Vol 199 (37-40), pp. 2559-2570.

[2] Cervera, M., Chiumenti, M., Codina, R. (2010) "Mixed stabilized finite element methods in nonlinear solid mechanics. Part II: Strain localization". *Computer Methods in Applied Mechanics and Engineering*, Vol 199 (37-40), pp. 2571-2589.

[3] Cervera, M., Chiumenti, M., Benedetti, L., Codina, R. (2015) "Mixed stabilized finite element methods in nonlinear solid mechanics. Part III: Compressible and incompressible plasticity". *Computer Methods in Applied Mechanics and Engineering*, Vol 285, 752-775.

[4] Soto, O.A., Baum, J.D., Löhner, R. (2010) "An efficient fluid-solid coupled finite element scheme for weapon fragmentation simulations". *Eng. Fracture Mech.*, Vol 77, 549-564.

[5] Badia, S., Codina, R., (2009) "Unified stabilized finite element formulation for the Stokes and the Darcy problem", *SIAM journal of Numerical Analysis*, Vol 17, 309-330.

[6] Soto, O., Löhner, R., Cebal, J., Camelli, F., (2004) "A stabilized edge-based implicit incompressible flow formulation. *Computer Methods in Applied Mechanics and Engineering*, Vol 293, 2139-2154.

[7] Flanagan, D., Belytschko, T., (1981) "A Uniform Strain Hexahedron and Quadrilateral with Orthogonal Hourglass Control". *International Journal for Numerical Methods in Engineering*, Vol 17, 679-706